Raman spectroscopy of f-electron metals: An example of CeB_6

Mai Ye,[1,*] H.-H. Kung,[1] Priscila F. S. Rosa,[2] Eric D. Bauer,[2] Zachary Fisk,[3] and Girsh Blumberg[1,4,†]

[1]*Department of Physics and Astronomy, Rutgers University, Piscataway, New Jersey 08854, USA*

[2]*Los Alamos National Laboratory, Los Alamos, New Mexico 87545, USA*

[3]*Department of Physics and Astronomy, University of California, Irvine, California 92697, USA*

[4]*National Institute of Chemical Physics and Biophysics, 12618 Tallinn, Estonia*

(Received 24 February 2019; published 14 June 2019)

We performed an optical spectroscopy study of electronic and magnetic excitations for a rare-earth system with a single electron quasilocalized in the f shell on an ion at high-symmetry crystallographic site in application to CeB_6 heavy-fermion metal. We carried out group-theoretical classification of the electronic crystal field (CF) transitions and assessed their coupling to light cross sections for polarization resolved Raman scattering processes. We discuss applicability of symmetrized Raman susceptibility to studies of exotic charge and spin high multiplet ordering phases in f-electron systems. We study temperature effects on intra- and intermultiplet CF transitions and also on the coupling between the CF excitations with the lattice vibrations. We acquired temperature dependence of the low-frequency polarization resolved Raman response for all Raman-allowed symmetry channels: A_{1g}, E_g, T_{1g}, and T_{2g} of the cubic O_h point group. We demonstrate that T_{1g}-symmetry static Raman susceptibility shows a temperature dependence which is consistent with the previously-reported magnetic susceptibility data. Such behavior in the T_{1g} channel signifies the presence of long wavelength magnetic fluctuations, which is interpreted as a manifestation of ferromagnetic correlations induced by tendency towards quadrupolar ordering.

DOI: 10.1103/PhysRevMaterials.3.065003

I. INTRODUCTION

Strongly correlated d- and f-electron systems support a rich variety of low-temperature phases, including magnetism and superconductivity [1–4]. Among these phases, long-range order of multipoles, namely high-rank electric or magnetic moments, has great interest [5–8]. For example, second-rank quadrupolar moments could lead to novel phenomena including the quadrupolar Kondo effect [9] and quadrupole-fluctuation-mediated superconductivity [10]. In d-electron systems, the orbital angular momentum is usually quenched by large crystal-field (CF) splitting, hindering multipolar moments. f-electron systems, on the other hand, are suitable choices to study multipolar interactions and ordering phenomena by virtue of the interplay of the spin and orbital degrees of freedom. Indeed, the actinide dioxides, in which $5f$ electrons play an important role, serve as a paradigm for understanding the physics of multipolar interactions [6]. Quadrupolar orderings have also been discovered in a number of $4f$-electron compounds [7,11–15].

CeB_6, with its simple chemical composition, lattice structure, and electronic configuration, is considered a prototypical example of heavy-fermion metal with quadrupolar ordering. This material has a cubic structure (space group $Pm\bar{3}m$, No. 221; point group O_h) composed of cerium ions and boron octahedrons [Fig. 1(a)]. Every Ce^{3+} ion has only one electron in its $4f$ orbital and O_h site symmetry. CeB_6 undergoes a second-order phase transition into a nonmagnetic phase at $T_Q = 3.2$ K, before developing an antiferromagnetic (AFM) order below $T_N = 2.3$ K [16,17]. The AFM phase has a double-Q commensurate magnetic structure with $Q_1 = (0.25, 0.25, 0)$ and $Q_2 = (0.25, 0.25, 0.5)$ [18,19]. As for the nonmagnetic phase, neutron scattering shows no structural transition at T_Q [19]. Resonant x-ray diffraction determines that this nonmagnetic phase involves an orbital ordering with wave vector (0.5, 0.5, 0.5) [20], and the C_{44} elastic constant, related to ϵ_{xy}-type strains, shows an anomaly at T_Q [21]. Based on these results, it is generally believed that the nonmagnetic phase is a two-sublattice arrangement of Ce^{3+} O_{xy}-type electric quadrupole moments, with a wave vector (0.5, 0.5, 0.5) [7]. This proposed antiferroquadrupolar (AFQ) model is consistent with experimental data in the presence of magnetic field [22–26], but to our knowledge, up to now there is no direct evidence demonstrating the O_{xy}-type AFQ order in zero field. A sketch of field-temperature phase diagram for CeB_6 is shown in Fig. 1(b).

All experimental results reported in this study correspond to the zero-field paramagnetic (PM) phase, namely, the data is acquired at $T > T_Q$.

In recent years multiple experimental studies have revealed the importance of unexpected ferromagnetic (FM) correlations in the low-temperature ordering phenomena of CeB_6. In the AFQ phase with finite magnetic field, electron spin resonance (ESR) with narrow linewidth was uncovered, pointing to existence of FM correlations [27]. Theoretical study suggested that such FM correlations result from AFQ ordering [26]. A zone-center excitation at the (110) point, following the energy of ESR, was found by inelastic neutron scattering

*mye@physics.rutgers.edu

†girsh@physics.rutgers.edu

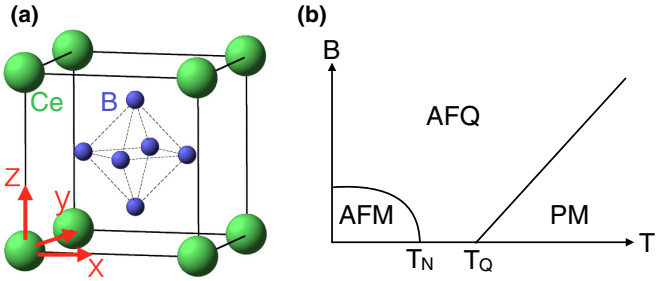

FIG. 1. (a) Crystal structure of CeB_6. (b) A sketch of field-temperature phase diagram for CeB_6.

(INS) [28]. In the AFQ phase at zero magnetic field, this finite-energy mode collapses into a quasielastic peak [29]. Moreover, intense FM fluctuations were uncovered in the AFM phase, suggesting propensity to FM instability [29].

Both the AFQ and AFM phases are closely related to the CF ground state [7]. In CeB_6, sixfold degenerate $^2F_{5/2}$ is the ground multiplet, and eightfold $^2F_{7/2}$ is the lowest-energy excited multiplet [Fig. 2]. These two multiplets were identified in photoemission spectroscopy studies [30,31] by the self-energy effects [32]. From group theory analysis [33], the cubic CF potential splits the $^2F_{5/2}$ multiplet into quartet Γ_8 and doublet Γ_7 states, and the $^2F_{7/2}$ multiplet into doublet Γ_6^*, doublet Γ_7^*, and quartet Γ_8^* states [34]. For the $^2F_{5/2}$ multiplet, the Γ_8 state is the ground state [35–38] and the Γ_7 state has an energy of 372 cm^{-1} at room temperature [36,39]. For the $^2F_{7/2}$ multiplet, the energy of the CF levels has not been determined experimentally.

In order to better understand the low-temperature ordering phenomena in CeB_6, a more detailed study of the interplay of CF excitations, lattice dynamics, and the FM correlations is required. Raman spectroscopy is a suitable technique providing symmetry-resolved excitation spectra of electronic, magnetic, and phononic degrees of freedom. As a photon-in-photon-out inelastic scattering process, polarization-resolved

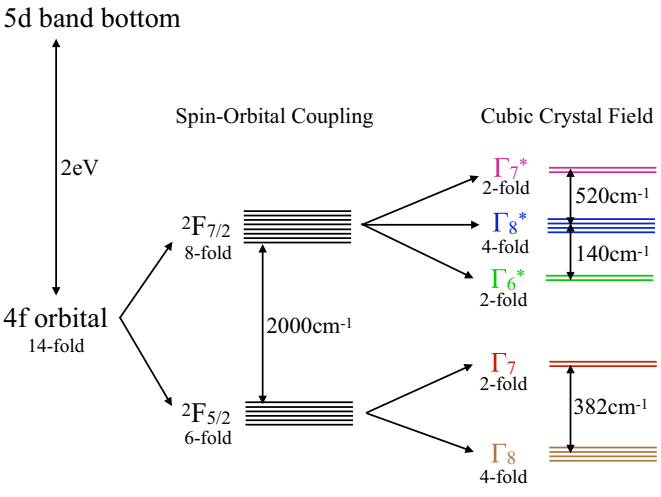

FIG. 2. Schematic energy diagram illustrating the splitting of $4f$ orbital by spin-orbital coupling and cubic crystal field. The same color scheme is used in Figs. 2, 5, 6, and 7 to identify the four crystal-field transitions.

Raman scattering has the unique advantage of high energy-resolution and the ability to disentangle the excitation spectra into individual symmetry channels. The symmetry of a particular excitation can be identified by controlling the polarization of the incident and scattered light [40]. This experimental method has been successfully used to study CF excitations [41,42]; it is a well-fitted choice of investigating the intra- and intermultiplet CF excitations of CeB_6. Moreover, Raman scattering makes it possible to study the excitations in the magnetic dipolar (T_{1g} of O_h group) and electric quadrupolar (E_g and T_{2g} of O_h group) channels separately. Thus, the relationship between the quadrupolar correlations and FM correlations can be clarified. Notice that quadrupolar excitations involve a change of the component of angular momentum along the quantization axis by two quantum units. Among conventional experimental probes, only photons can induce quadrupolar excitations.

In this paper, we present a comprehensive study of CeB_6 using optical secondary-emission spectroscopy. We identify an intense photoluminescence feature corresponding to $5d-4f$ recombination process. We analyze the temperature dependence of both intra- and intermultiplet CF excitations and illustrate the interaction between light and CF states by a model Hamiltonian calculation. We draw information about the electron-phonon interaction by studying lattice dynamics. We observe dynamical magnetic fluctuations related to the ordered broken-symmetry states. Especially, we demonstrate two virtues of Raman scattering which have not been generally appreciated: First, the temperature dependence of the parameters of CF excitations reveals the interaction between f-electrons and itinerant electrons; second, the low-energy Raman response probes dynamical fluctuations related to exotic multipolar ordering.

The rest of this paper is organized as follows. In Sec. II we describe the sample preparation and experimental setup. In Sec. III we present and discuss the experimental results; in this section, we first show an overview of the main spectral features in Sec. III A and then discuss them separately in the following subsections. In Sec. III B we show the high-energy photoluminescence (CF) feature. In Sec. III C we discuss the CF excitations. Specifically, in III C 1 we present the four lowest-energy CF excitations of Ce^{3+} ions and identify the symmetry of the CF states; in III C 2, we analyze the temperature dependence of the CF parameters and explain the observed anomaly on the basis of Kondo effect; in III C 3, we build a single-ion Hamiltonian and fit the measured CF energies with this Hamiltonian to evaluate the SOC and CF strength and to obtain the wave functions of eigenstates. In Sec. III D we discuss lattice dynamics. The asymmetric lineshape and relatively large full width at half maximum (FWHM) of the optical phonon modes point to electron-phonon interaction. In Sec. III E we discuss quasielastic excitations. We find that quasielastic fluctuations in the symmetry channel containing magnetic excitations develops below 20 K and that the temperature dependence of the corresponding Raman susceptibility is consistent with the previously-reported static magnetic susceptibility data. Finally, in Sec. IV we provide a summary of our observations and their implications.

TABLE I. The relationship between the scattering geometries and the symmetry channels. Every scattering geometry is represented by E_iE_s, where E_i and E_s are the polarizations of incident and scattered light; X, Y, X', and Y' are the [100], [010], [110], and [1$\bar{1}$0] crystallographic directions; R and L are right and left circular polarizations. A_{1g}, E_g, T_{1g}, and T_{2g} are the irreducible representations of the O_h group.

Scattering geometry	Symmetry channel
XX	$A_{1g} + 4E_g$
XY	$T_{1g} + T_{2g}$
$X'X'$	$A_{1g} + E_g + T_{2g}$
$X'Y'$	$3E_g + T_{1g}$
RR	$A_{1g} + E_g + T_{1g}$
RL	$3E_g + T_{2g}$

II. EXPERIMENTAL

Single crystals of CeB_6 were grown in Al flux by slow cooling from 1450 °C. The crystals were removed from the Al flux by leaching in NaOH solution [43,44]. The sample measured in this study was cleaved in ambient condition to expose its (001) crystallographic plane; the cleaved surface was then examined under a Nomarski microscope to find a strain-free area.

Raman-scattering measurements were performed in a quasibackscattering geometry from a sample placed in a continuous helium-gas-flow cryostat. A set of lines from a Kr^+ ion laser, 476, 531, 647, 676, and 752 nm, were used for excitation. Incident light with less than 10 mW power was focused into a 50×100 μm^2 spot. The temperature points reported in this paper were corrected for laser heating, which was estimated to be 0.5 K/mW [45].

Six polarization configurations were employed to probe excitations in different symmetry channels. The relationship between the scattering geometries and the symmetry channels [40] is given in Table. I. The algebra used to decompose measured spectra into four symmetry channels is shown in Table. II.

We used a custom triple-grating spectrometer with a liquid-nitrogen-cooled charge-coupled device (CCD) detector for analysis and collection of the scattered light. Low-resolution gratings with 150 lines per mm were used to measure the broad PL feature, while high-resolution gratings with 1800 lines per mm were used for measurements of the sharp Raman features. The data were corrected for the spectral response of the system.

TABLE II. The algebra used in this study to decompose the data into four symmetry channels.

Symmetry channel	Expression
A_{1g}	$(1/3)(XX + X'X' + RR - X'Y' - RL)$
E_g	$(1/6)(X'Y' + RL - XY)$
T_{1g}	$(1/2)(XY + RR - X'X')$
T_{2g}	$(1/2)(XY + RL - X'Y')$

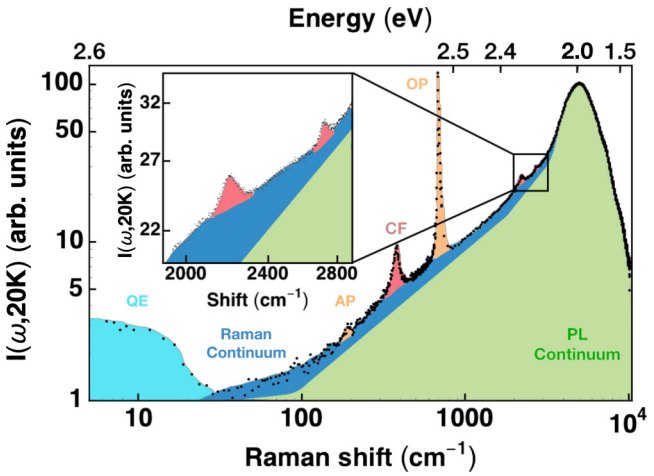

FIG. 3. An overview of the low-temperature secondary-emission intensity measured in XY geometry at 20 K with 476 nm excitation in log-log scale. The top scale is the absolute energy of the secondary-emission photons in electron-Volts. The bottom scale is the energy loss, the laser-photon energy minus the scattered-photon energy, also called the Raman shift, in spectroscopic units cm^{-1}. The Raman features are superposed on a strong photoluminescence continuum. Different Raman features are schematically represented by different colors: cyan, quasielastic (QE) Raman excitations; blue, the continuum of electronic Raman excitations; orange, second-order acoustic-phonon (AP) excitations and first-order optical-phonon (OP) excitations; red, crystal-field (CF) excitations; green: the continuum of the photoluminescence (PL).

For first-order scattering processes, the measured secondary-emission intensity $I(\omega, T)$ is related to the Raman response $\chi''(\omega, T)$ by $I(\omega, T) = [1 + n(\omega, T)]\chi''(\omega, T) + L(\omega, T)$, where n is the Bose factor, ω is excitation energy, T with temperature, and $L(\omega, T)$ represents photoluminescence [46]. For the second-order acoustic-phonon scattering process to be discussed in Sec. III D, assuming the two constitute excitations have the same energy, $I(\omega, T)$ and $\chi''(\omega, T)$ are related by $I(\omega, T) = [1 + n(\omega/2, T)]^2\chi''(\omega, T) + L(\omega, T)$ [46].

III. RESULTS AND DISCUSSION

A. Overview

In Fig. 3 we present a typical secondary-emission spectrum over a large energy range, covering Raman features of distinct origins. Among the Raman features, quasielastic excitations have the lowest energy. Second-order acoustic phonon excitations are at around 200 cm^{-1}, while first-order optical phonon excitations are near 1000 cm^{-1}. The energy of the intramultiplet CF excitation is around 400 cm^{-1}, while that of the intermultiplet CF excitations is more than 2000 cm^{-1}. The PL continuum arises from a broad PL peak at around 2.0 eV. In the following subsections we will discuss every spectral feature separately in detail.

B. Photoluminescence

In Fig. 4(a) we show the excitation dependence of the PL feature at room temperature. The PL peak has 2.0 eV

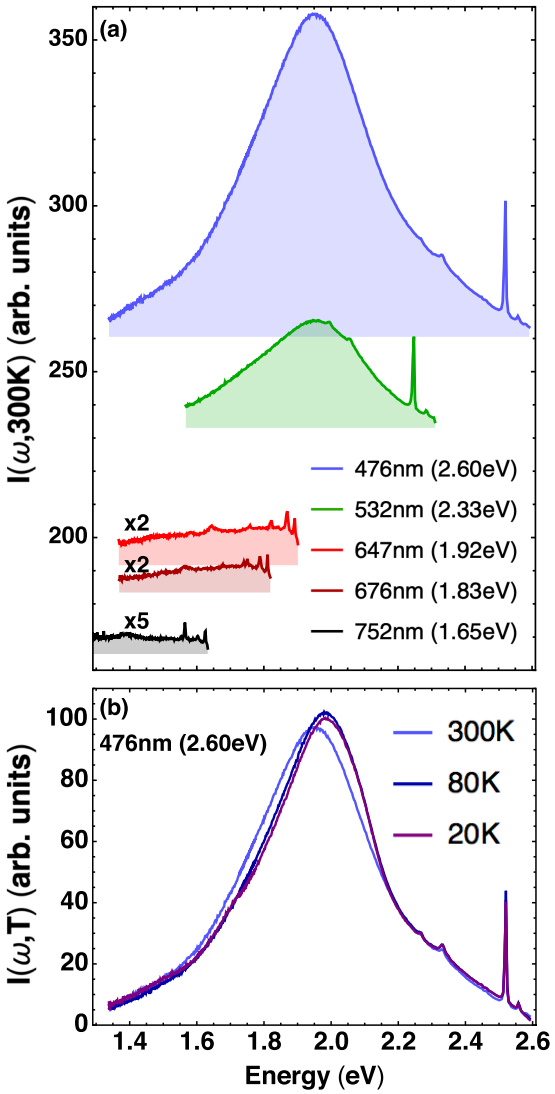

FIG. 4. (a) Excitation dependence of the secondary-emission intensity I(ω, 300 K) measured in XY geometry at 300 K. For clarity, each spectrum is vertically shifted by a factor proportional to the excitation energy. The broad peak which does not change in the absolute emission energy with excitation energy is a photoluminescence feature, while the sharp modes which follow the excitation energy are the Raman features. (b) Temperature dependence of the photoluminescence feature measured in XY geometry with 476 nm excitation.

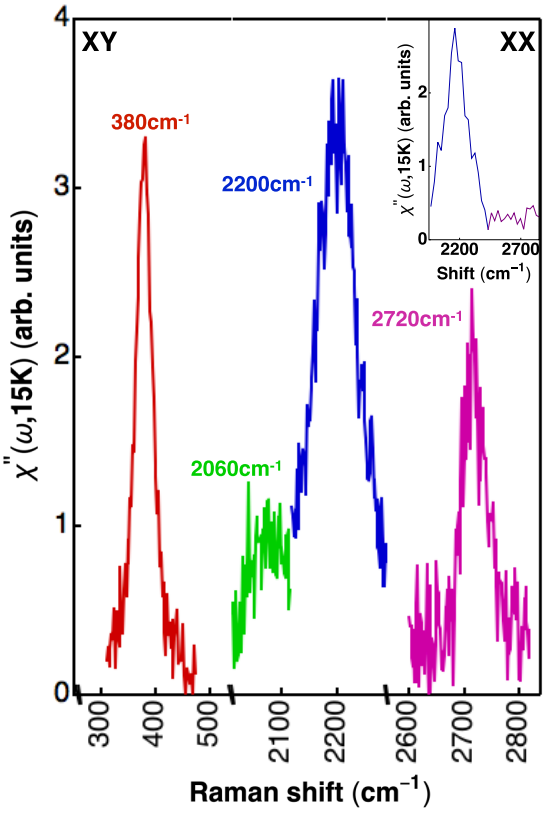

FIG. 5. Raman response $\chi''(\omega, 15\ \mathrm{K})$ of the CF excitations measured in XY scattering geometry ($T_{1g} + T_{2g}$) with 476 nm excitation at 15 K. Three axis breakers are used on the horizontal axis in order to show the four excitations together. The spectral resolution is 3.5 cm^{-1}. Inset: $\chi''(\omega, 15\ \mathrm{K})$ measured in XX scattering geometry ($A_{1g} + 4E_g$) at 15 K. The spectral resolution of the inset is about 30 cm^{-1}.

excitation threshold, and excitations below 2.0 eV threshold show predominantly Raman features. The PL feature is centered at 1.95 eV, just below the threshold energy, and has about 0.4 eV full width at half maximum (FWHM). Upon cooling the peak shifts slightly to higher energy [Fig. 4(b)].

The optical conductivity shows a shoulder at around 2.0 eV [47–49], suggesting an optical gap. Band-structure calculations further indicate a 2.0 eV gap between the Ce dispersive 5d-band bottom and flat 4f band [50–52]. We therefore attribute the PL peak to the recombination of the electron-hole excitations between the 5d and 4f bands. Transitions between d and f states are dipole allowed, and the energy separation of the 5d-band bottom and the 4f band is consistent with the energy of this PL peak. The enhancement of PL intensity for excitations above the 2 eV threshold results from the increase of the density of states (DOS) for the 4f to 5d interband transition.

C. Crystal-field excitations

1. Identification

In total, there are four CF excitations from the Γ_8 ground state to the higher states within the $^2F_{5/2}$ and $^2F_{7/2}$ multiplets: one intramultiplet excitation and three intermultiplet excitations (Fig. 2). In Fig. 5 we present the spectrum of the four CF excitations measured at 15 K. Four peaks at 380 cm^{-1}, 2060 cm^{-1}, 2200 cm^{-1}, and 2720 cm^{-1} are observed. The 380 cm^{-1} excitation is the intramultiplet $\Gamma_8 \rightarrow \Gamma_7$ transition. Among the three intermultiplet excitations, only the $\Gamma_8 \rightarrow \Gamma_8^*$ transition can have a finite A_{1g} component [33]. In the inset of Fig. 5 we show that among the intermultiplet excitations only the one at 2200 cm^{-1} contains an A_{1g} component. The 2200 cm^{-1} excitation is therefore assigned to the $\Gamma_8 \rightarrow \Gamma_8^*$ transition. The CF excitation at 2720 cm^{-1}, in turn, can only be a transition between the Γ_8 ground state and the Γ_6^* or Γ_7^* states. Raman scattering cannot distinguish between $\Gamma_8 \rightarrow \Gamma_6^*$ and $\Gamma_8 \rightarrow \Gamma_7^*$ transitions because they both contain

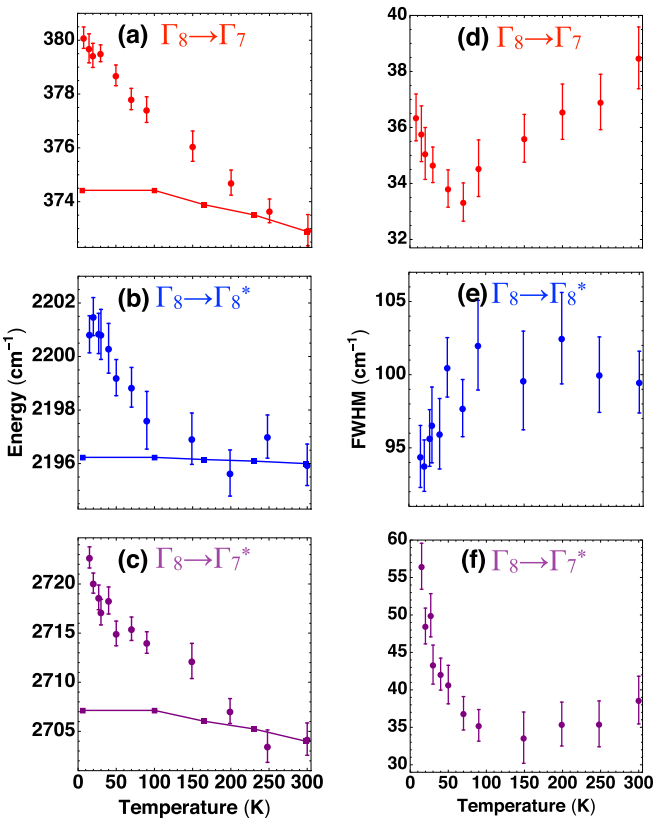

FIG. 6. Temperature dependence of the energy (a)–(c) and FWHM (d)–(f) of the $\Gamma_8 \rightarrow \Gamma_7$, $\Gamma_8 \rightarrow \Gamma_8^*$, and $\Gamma_8 \rightarrow \Gamma_7^*$ CF excitations shown in Fig. 5. The line-joined square labels in (a)–(c) represent the excitation energies calculated by our model Hamiltonian calculation. The error bars represent one standard deviation of the Lorentzian fit.

the same irreducible representations [33]: $\Gamma_8 \otimes \Gamma_6^* = \Gamma_8 \otimes \Gamma_7^* = E_g \oplus T_{1g} \oplus T_{2g}$. However, we will show in Sec. III C 3 that the electron-cloud distribution of the Γ_6^* state has the smallest overlap with the boron octahedrons, the Γ_8^* state has intermediate overlap, and the Γ_7^* state has the largest overlap. Because of the Coulomb repulsion between cerium and boron electrons, the Γ_7^* state has the highest energy while the Γ_6^* state has the lowest energy. Indeed, within the $^2F_{5/2}$ multiplet because the Γ_7 state has more overlap with the boron octahedrons it has a higher energy than the Γ_8 state. Therefore, the 2720 cm^{-1} excitation is assigned to the $\Gamma_8 \rightarrow \Gamma_7^*$ transition, and the 2060 cm^{-1} excitation is assigned to the $\Gamma_8 \rightarrow \Gamma_6^*$ transition.

2. Temperature dependence

In Fig. 6 we present the temperature dependence of the energy and FWHM of three CF excitations. The spectral parameters of the CF excitations were obtained by fitting the measured spectral peaks with a Lorentzian lineshape.

On cooling from 304 K to 15 K the lattice contraction strengthens the electrostatic potential at the Ce sites resulting in increase of the $\Gamma_8 \rightarrow \Gamma_7$, $\Gamma_8 \rightarrow \Gamma_8^*$, and $\Gamma_8 \rightarrow \Gamma_7^*$ transition energy by 7 cm^{-1}, 5 cm^{-1}, and 18 cm^{-1}, respectively [53]. A discussion of the change of the energy of the CF states with increasing CF potential will be given in Sec. III C 3.

At room temperature, the CF spectral lines of CeB_6 are broader than those measured from Ce^{3+} ions embedded in insulators, e.g., Ce-doped Y_2O_3 [54] or Ce-doped $LuPO_4$ [55]. The broadening could be caused by two factors: First, lattice of Ce^{3+} ions leads to small dispersion of the narrow $4f$ bands; second, hopping of conduction electrons among the boron sites induces fluctuations of the electrostatic potential at the Ce sites, which broadens FWHM.

On cooling, the FWHM of the $\Gamma_8 \rightarrow \Gamma_7$ and $\Gamma_8 \rightarrow \Gamma_7^*$ CF transitions decrease from 300 K to 80 K but anomalously increases below 80 K [Figs. 6(d) and 6(f)]. The decrease of FWHM is expected because lattice vibrations, causing fluctuations of the electrostatic potential at Ce sites, diminish with cooling. In order to understand the anomalous increase of FWHM below 80 K, it is important to notice that the electrical resistivity of CeB_6 has its local minimum at 80 K. The resistivity upturn below 80 K results from the Kondo effect [16] due to increase in the rate of conduction electron scattering from the local moments at the Ce sites on cooling [56,57]. The Kondo effect shortens the lifetime of the Γ_7 and Γ_7^* CF states, so the FWHM of the $\Gamma_8 \rightarrow \Gamma_7$ and $\Gamma_8 \rightarrow \Gamma_7^*$ CF transition increases below 80 K. Nevertheless, the FWHM of the $\Gamma_8 \rightarrow \Gamma_8^*$ CF transition does not show an upturn below 80 K [Fig. 6(e)]. This is because the Γ_8^* state has smaller overlap with the boron octahedrons than the Γ_7 and Γ_7^* states, therefore, it is less influenced by the increased conduction electron scattering rate.

Our data do not display directly the splitting of the Γ_8 CF ground state. However, the minimum FWHM of the $\Gamma_8 \rightarrow \Gamma_7$ is around 33 cm^{-1} [Fig. 6(d)]: If the splitting of the CF ground state is small, it would not be resolved. The previous studies suggested a splitting of 20 cm^{-1} [36,58], which does not contradict our data.

3. Model Hamiltonian calculation

To shed light on the nature of the CF transitions, we perform a model Hamiltonian calculation. We use the following single-ion Hamiltonian

$$H = E_0 + H_{\mathrm{SOC}} + H_{\mathrm{CF}}. \tag{1}$$

The first term E_0 represents the energy of unperturbed $4f$ shell. The value E_0 is chosen to put the Γ_8 ground state at zero energy. The second term

$$H_{\mathrm{SOC}} = \xi \hat{\mathbf{L}} \cdot \hat{\sigma} \tag{2}$$

describes the effect of SOC. Here ξ is the SOC coefficient, $\hat{\mathbf{L}}$ is the orbital angular momentum operator, and $\hat{\sigma}$ are Pauli matrices. The third term

$$H_{\mathrm{CF}} = B_4\left(\hat{O}_4^0 + 5\hat{O}_4^4\right) + B_6\left(\hat{O}_6^0 - 21\hat{O}_6^4\right) \tag{3}$$

is the general expression for a CF potential of cubic site symmetry [59], where $\hat{O}_4^0$, $\hat{O}_4^4$, $\hat{O}_6^0$, and $\hat{O}_6^4$ are Stevens operators [60], and B_4 and B_6 are the CF coefficients [61]:

$$B_4 = A_4\langle r^4\rangle\beta, \tag{4}$$

$$B_6 = A_6\langle r^6\rangle\gamma. \tag{5}$$

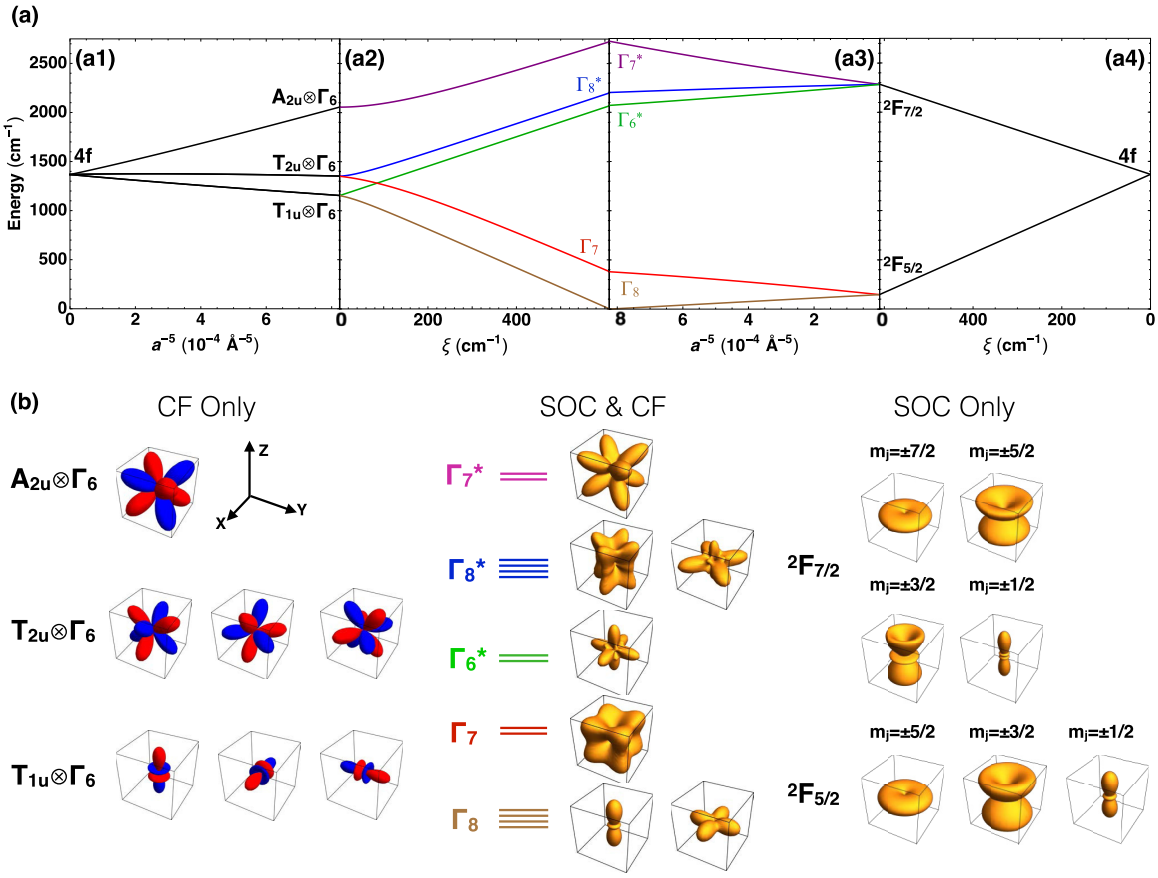

FIG. 7. Eigenenergies and eigenstates derived from the model Hamiltonian calculation. (a) Evolution of the $4f$-orbital energy with CF potential and SOC strength. (From left to center) Increasing CF potential in the absence of SOC (a1) and then increasing SOC strength in the existence of full CF potential (a2); increasing SOC in the absence of CF potential (a3) and then increasing CF potential in the existence of full SOC (a4). In this panel, the full SOC strength is $\xi = 610$ cm^{-1}, and the full CF potential strengths are $B_4 = -0.758$ cm^{-1} and $B_6 = -0.0165$ cm^{-1}. (b) The wave functions and the angular electron-cloud distribution of the eigenstates. (Left) The wave functions of the eigenstates when only CF potential is present. Red denotes positive value while blue denotes negative value; (middle) the angular electron-cloud distribution of the eigenstates when both SOC and CF potential are present; (right) the angular electron-cloud distribution of the eigenstates when only SOC is present.

A_4 and A_6 are the geometrical coordination factors determined by the charge configuration around the Ce sites. Regardless of the specific configuration, A_4^{-5} and A_6^{-7}, where a is the lattice constant; $\langle r^4\rangle$ and $\langle r^6\rangle$ are the mean fourth and sixth powers of the radii of the Ce^{3+} $4f$ orbital, and β and γ are the Stevens multiplicative factors [60].

The effects of SOC and CF potential on the energy and angular electron-cloud distribution of the CF levels are illustrated in Fig. 7. In the absence of the SOC, the CF eigenfunctions could be classified by the irreducible representations (IRs) of O_h double group. The relevant IRs are the one-dimensional A_{2u}, three-dimensional T_{2u}, and three-dimensional T_{1u} for the orbital part of the wave function, and two-dimensional Γ_6 for the spin part. The 14-fold degenerate $4f$ orbital would be split into twofold $A_{2u}\otimes\Gamma_6$, sixfold $T_{2u}\otimes\Gamma_6$, and sixfold $T_{1u}\otimes\Gamma_6$ orbitals. Finite SOC splits further these orbitals and results in mixing of wave functions derived from different orbitals. The symmetry of the split states is given by the decomposition of the direct products into direct sums of IRs of O_h double group [33]: $A_{2u}\otimes\Gamma_6 = \Gamma_7$, $T_{2u}\otimes\Gamma_6 = \Gamma_8\oplus\Gamma_7$, and $T_{1u}\otimes\Gamma_6 = \Gamma_6\oplus\Gamma_8$.

On the other hand, if cubic CF were absent, the $4f$ orbital would be split into eightfold $^2F_{7/2}$ ($J = L + S$) and sixfold $^2F_{5/2}$ ($J = L - S$) multiplets. Finite CF potential splits the two multiplets and induces mixing of wave functions derived from different multiplets [46]. The symmetry of the split states is given by the compatibility table showing the mapping of IRs of the full rotational group into IRs of O_h double group [33]: $^2F_{7/2} = \Gamma_8\oplus\Gamma_7\oplus\Gamma_6$, and $^2F_{5/2} = \Gamma_8\oplus\Gamma_7$. With both SOC and CF present, the CF eigenfunctions should be classified by the IRs of the double group, namely two-dimensional Γ_6, two-dimensional Γ_7, and four-dimensional Γ_8.

We diagonalize the Hamiltonian (1) in the basis of $|L, m_l\rangle|S, m_s\rangle$, where L, m_l, S, m_s are quantum numbers corresponding to $\hat{\mathbf{L}}, \hat{L}_z, \hat{\mathbf{S}}, \hat{S}_z$ operators, respectively. After diagonalization, the CF transition energies can be expressed in terms of ξ, B_4, and B_6. We obtain these three parameters by fitting the energies of three CF transitions to the data at 15 K (the weakest $\Gamma_8\rightarrow\Gamma_6^*$ transition is not accounted for in this procedure). The obtained set of parameters comprises $\xi = 610$ cm^{-1}, $B_4 = -0.758$ cm^{-1}, and $B_6 = -0.0165$ cm^{-1}. The same values automatically render the energy of weakest transition at 2070 cm^{-1}, which is close to

the observed value at 2060 cm^{-1}. The value of ξ (610 cm^{-1}) is also consistent with the estimated value for the Ce^{3+} ion embedded in $LuPO_4$ (614 cm^{-1}) [55]. Such consistency demonstrates the reliability of the model (1).

We can further use this single-ion model to describe the temperature dependence of the CF excitation energy. Here we assume that ξ is temperature independent and that the temperature dependence of the B_4 and B_6 coefficients comes from the temperature dependence of the lattice constant $a(T)$. We therefore rewrite B_4 and B_6 as $B_4(T) = C_4 a(T)^{-5}$ and $B_6(T) = C_6 a(T)^{-7}$, where C_4 and C_6 are temperature-independent factors. The temperature dependence of the lattice constant $a(T)$ is obtained from the Refs. [19,62]. Then, we determine the values of ξ, C_4, and C_6 by matching the calculated values with the measured data at 300 K. Finally, we use the determined ξ, C_4, and C_6 to calculate CF excitation energies below 300 K. The results are shown in Figs. 6(a)–6(c). The discrepancy between the measured data and the calculated values below 200 K results from unaccounted for terms in the model Hamiltonian [Eq. (1)]; for an example, interactions between localized f-electrons and the itinerant conduction electrons.

By virtue of the obtained eigenfunctions, the Raman intensity of the four CF transitions can be calculated. For nonresonant scattering, the Raman response $\chi''(\omega)$ has the following expression [63]:

$$\chi''(\omega) \sim \frac{1}{Z}\sum_{i,f} |\langle f|\hat{R}_{\mu\nu}|i\rangle|^2 e^{-E_i/kT}\delta(E_f - E_i - \hbar\omega), \quad (6)$$

where Z is the partition function, $|i\rangle$, $|f\rangle$ are the initial and final state with energy E_i and E_f, ω is the Raman shift, and $\hat{R}_{\mu\nu}$ is the effective Raman operator. In our case, $|i\rangle$ is the CF ground state and $|f\rangle$ is one of the excited CF states. For nonresonant Raman scattering, $\hat{R}_{\mu\nu}$ is a quadrupolar operator depending on the crystallographic symmetry and scattering geometry $\mu\nu$ [55,64,65]. For XY scattering geometry in a cubic crystal, $\hat{R}_{XY}$ transforms in the same way as quadrupole xy under the symmetry operations of O_h point group:

$$\hat{R}_{XY} = \frac{1}{2}(\hat{L}_x\hat{L}_y + \hat{L}_y\hat{L}_x) = \frac{1}{4i}(\hat{L}_+^2 - \hat{L}_-^2), \quad (7)$$

where $\hat{L}_+$ and $\hat{L}_-$ are the ladder operators of the orbital angular momentum. We note that because light only couples to the electron's orbital degree of freedom, the effective Raman operator should be written in terms of the orbital angular momentum operators, rather than the total angular momentum operators. Expression (7) should accordingly be evaluated in the basis of $|L, m_l\rangle|S, m_s\rangle$.

In Fig. 8 we compare the calculated and measured CF transition intensity. Because the 476 nm excitation is resonant with interband transitions (see Sec. III B) but the expression (7) is only valid for nonresonant scattering, we expect discrepancy between the calculated and measured results. Nevertheless, the relative intensity of the three intermultiplet transitions is reproduced.

D. Phononic excitations

An overview of the phonon modes is presented in Fig. 9(a). From group-theory analysis, CeB_6 has three Raman-active optical phonon modes: A_{1g}, E_g, and T_{2g}. Their respective energies are 1271, 1143, and 681.7 cm^{-1} at 300 K, consistent with previous results [66,67]. Their lineshapes at 300 K and 4 K are presented in Fig. 9(b); no anomaly is observed on cooling. The E_g and T_{2g} optical phonon modes exhibits asymmetric lineshape. The underlying electronic continuum likely results from electronic interband transitions: According to the calculated and measured band structure [50–52], many direct interband transitions are allowed and in turn can contribute to the nearly flat continuum below 1500 cm^{-1} (~0.2 eV).

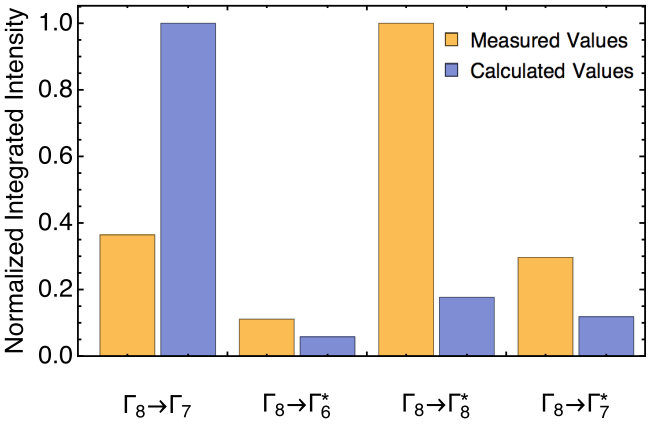

FIG. 8. Normalized intensity of the four CF transitions in XY scattering geometry at 15 K, measured (in yellow) and calculated (in blue). The measured/calculated intensity of the four transitions is normalized by their respective largest value.

The peak at 194 cm^{-1} is not fully polarized. It originates from second-order scattering of acoustic branches at the Brillouin-zone boundary [67], where the flat dispersion gives rise to a large density of states. From this peak, we infer that the maximum of the acoustic phonon frequency is around 100 cm^{-1}, which is consistent with the INS data [68]. Another feature at 373 cm^{-1} shows larger T_{2g} contribution and smaller E_g contribution. It is the $\Gamma_8 \rightarrow \Gamma_7$ CF excitation discussed in Sec. III C. The peak at 1400 cm^{-1} has strong A_{1g} contribution and very weak E_g contribution. It results from second-order scattering of the T_{2g} phonon mode [67]. The symmetry-decomposed spectra further reveal an A_{1g} peak at 1158 cm^{-1}, which was not reported previously. This peak might correspond to the summation mode of the 373 cm^{-1} CF excitation and the T_{2g} phonon mode. Such coupling has been observed in another f-electron system UO_2 [69].

In Fig. 10 we show the temperature dependence of the energy and FWHM of the A_{1g} contribution of the second-order acoustic mode and the A_{1g} optical mode. The spectral parameters of the phonon modes were obtained by fitting the measured spectral peaks with a Lorentzian lineshape.

Temperature dependence of the phonon energy and FWHM is usually described by anharmonic effects. In most cases, the three-phonon processes render the fastest relaxation, and higher-order processes can be neglected. Furthermore, the A_{1g} optical mode at the Γ point has the highest frequency among all the phonon branches of CeB_6 [72]; hence we only need to consider processes in which one A_{1g} optical mode at Γ point decays into two phonon modes satisfying conservation of energy and momentum [73]. We use a

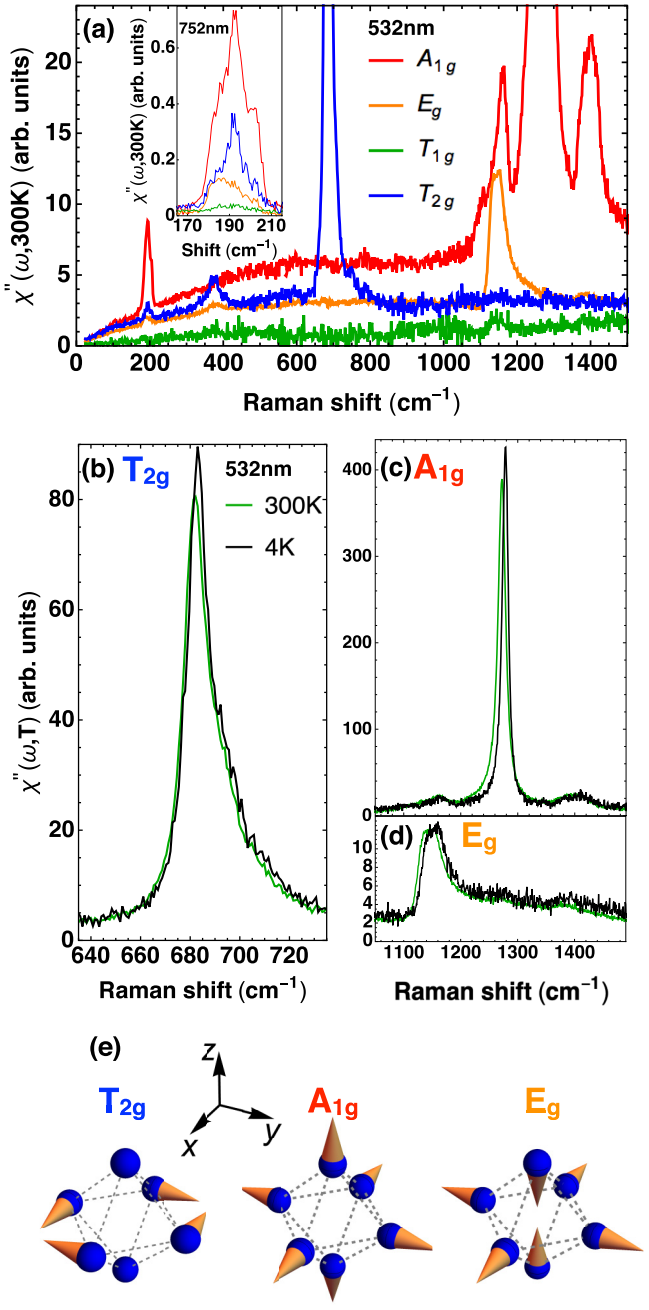

FIG. 9. (a) Symmetry-decomposed Raman response $\chi''(\omega, 300\,\mathrm{K})$, measured with 532 nm excitation at 300 K. Inset in (a): Symmetry-decomposed Raman spectrum of the second-order acoustic phonon scattering peak, measured with 752 nm excitation at 300 K. Thermal factor $[1+n(\omega/2,T)]^2$ is used to derive this particular inset; the other Raman spectra presented in this paper are obtained with the normal thermal factor $[1+n(\omega,T)]$. (b), (c), and (d): Raman spectra of the T_{2g}, A_{1g}, and E_g optical phonon modes, measured with 532 nm excitation at 300 K and 4 K. In (b), (c), and (d), the spectral resolution is 2.8 cm^{-1} for the high temperature data and 1.3 cm^{-1} for the low temperature data. (e) The schematic vibration patterns for the three optical phonon modes. Because the cerium ions are at the inversion centers, Raman-active phonon modes only involve vibrations of the boron octahedrons.

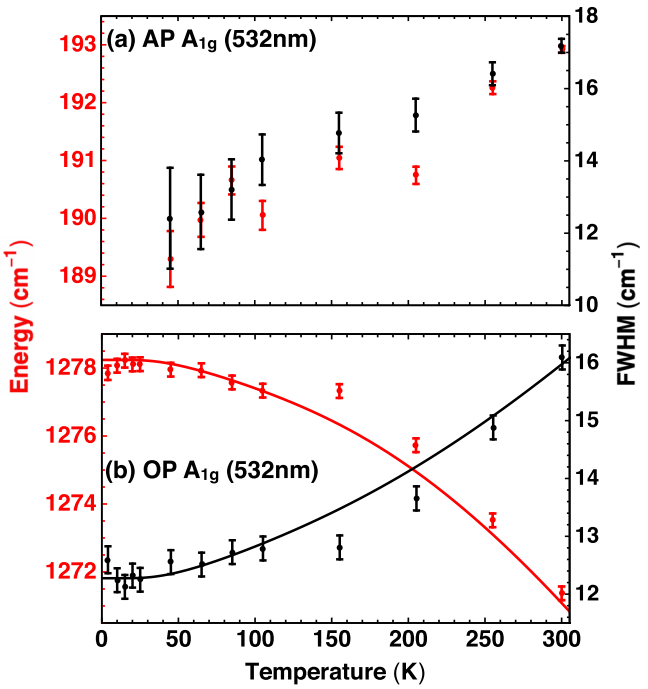

FIG. 10. Temperature dependence of the energy (in red) and FWHM (in black) of (a) the A_{1g} component of the second-order acoustic phonon scattering peak, and (b) the A_{1g} optical phonon mode. The solid lines are fitting curves of an anharmonic decay model assuming decay into two optical modes, or an optical plus an acoustic mode [70,71]. The error bars represent one standard deviation of the Lorentzian fit.

generalized anharmonic decay model assuming multiple decay channels; for every channel, the decay products can be two acoustic modes, an optical plus an acoustic mode, or two acoustic modes [70,71] [74]:

$$\omega(T) = \omega_0 - \sum_i \omega_{\delta(i)}\left[1+\frac{1}{e^{\hbar\omega_{1(i)}/k_BT}-1}+\frac{1}{e^{\hbar\omega_{2(i)}/k_BT}-1}\right], \tag{8}$$

$$\Gamma(T) = \Gamma_0 + \sum_i \Gamma_{\delta(i)}\left[1+\frac{1}{e^{\hbar\omega_{1(i)}/k_BT}-1}+\frac{1}{e^{\hbar\omega_{2(i)}/k_BT}-1}\right], \tag{9}$$

where the subscript (i) indicates the decay channel. $\omega_{\delta(i)}$ and $\Gamma_{\delta(i)}$ are factors reflecting the relative importance of the various decay channels. $\hbar\omega_{1(i)}$ and $\hbar\omega_{2(i)}$ are the energy of the decay products in the decay channel labeled by (i). $\hbar(\omega_0 - \sum_i \omega_{\delta(i)})$ and $\Gamma_0 + \sum_i \Gamma_{\delta(i)}$ correspond to the zero-temperature phonon energy and the FWHM, respectively. Γ_0 accounts for the temperature-independent part of the FWHM originating not from anharmonic decay processes but from, for example, imperfection of the sample. Both $\omega_{\delta(i)}$ and $\Gamma_{\delta(i)}$ are proportional to

$$\sum_{\mathbf{k}_{1(i)},\mathbf{k}_{2(i)}} |\alpha(\mathbf{k}_{1(i)},\mathbf{k}_{2(i)})|^2 \delta\left[\omega_{A_{1g}} - \omega_{1(i)}(\mathbf{k}_{1(i)}) - \omega_{2(i)}(\mathbf{k}_{2(i)})\right], \tag{10}$$

TABLE III. The fitting parameters for the energy and FWHM of the A_{1g} optical phonon mode. Units are cm^{-1}.

ω_0	$\omega_{\delta(1)}$	$\omega_{\delta(2)}$
1309.0 ± 0.1	28.12 ± 0.05	2.664 ± 0.003
Γ_0	$\Gamma_{\delta(1)}$	$\Gamma_{\delta(2)}$
1.07 ± 0.08	8.4 ± 0.2	1.76 ± 0.01

where α is the anharmonic coefficient; $\mathbf{k}_{1(i)}$ and $\mathbf{k}_{2(i)}$ are the wave vector of the decay products in the decay channel labeled by (i); δ represents the Dirac δ function.

Referring to the calculated phonon dispersion [72], we expect two decay channels for the 1278 cm^{-1} A_{1g} phonon: (1) decay into one 684 cm^{-1} optical phonon and one 594 cm^{-1} optical phonon with opposite momenta; (2) decay into one 1178 cm^{-1} optical phonon near the +R point and one 100 cm^{-1} acoustic phonon near the −R point.

The two phonon branches involved in the decay channel (1) are essentially flat over the whole Brillouin zone; hence a large number of states are available for the decay to happen. On the contrary, for the two phonon branches of the decay channel (2), only states near the R point simultaneous satisfy the requirements of energy and momentum conservation. Therefore, the decay channel (1) would dominate if the anharmonic coefficient is not significantly different for the two channels.

The fitting results of the anharmonic decay model are summarized in Table III. Indeed, $\omega_{\delta(1)} > \omega_{\delta(2)}$ and $\Gamma_{\delta(1)} > \Gamma_{\delta(2)}$. The temperature-independent Γ_0 is much smaller than $\Gamma_{\delta(1)} + \Gamma_{\delta(2)}$, indicating not only that the lineshape broadening mainly results from the anharmonic decay but also that the sample is of excellent quality. In contrast to the behavior of the A_{1g} optical mode, the second-order scattering of acoustic modes in the A_{1g} channel shows decreasing energy on cooling [Fig. 10(a)]. The 2% softening might be a prelude to the AFQ ordering.

We attribute the apparent asymmetric lineshape of the T_{2g} and E_g optical phonon modes to the coupling between these phonons and the low-frequency fluctuations (Sec. III E). The observed spectral lineshapes are resulted from convolution of the phononic Lorentzian and Drude-like function describing the low-lying fluctuations. We use the following expression to fit modes' lineshape at 4 K:

$$\begin{aligned}\chi''(\omega, 4K) &= \sum_i \Bigg\{ \frac{A_{(i)}^2 \gamma_{L(i)}}{(\omega - \omega_{L(i)})^2 + \gamma_{L(i)}^2} \\ &+ \frac{A_{(i)}^2 v_{(i)} \theta(\omega - \omega_{L(i)})(\omega - \omega_{L(i)})[1 + n(\omega - \omega_{L(i)}, 4K)]}{(\omega - \omega_{L(i)})^2 + (\gamma_{L(i)} + \gamma_{D(i)})^2} \\ &+ \frac{A_{(i)}^2 v_{(i)} \theta(\omega_{L(i)} - \omega)(\omega_{L(i)} - \omega) n(\omega_{L(i)} - \omega, 4K)}{(\omega_{L(i)} - \omega)^2 + (\gamma_{L(i)} + \gamma_{D(i)})^2} \Bigg\}. \end{aligned} \tag{11}$$

In Eq. (11), the first term describes the bare phonon part, while the second and third terms correspond to the Stokes and anti-Stokes of the phonon assisted electronic scattering. The summation runs over all the k points in the Brillouin zone. Referring to the calculated phonon dispersion [72], the T_{2g} mode belongs to a flat branch over the Brillouin zone, while the E_g mode belongs to a dispersive branch which has high DOS at Γ and R points [72]. Therefore, for the latter case we only consider coupling at Γ and R points. In this equation, $A_{(i)}$ is the phonon light-scattering vertex; $\omega_{L(i)}$ is the phonon frequency; $2\gamma_{L(i)}$ is the FWHM of the bare phonon Lorentzian function; γ_{Di} measures the relaxation rate of the Drude function; $v_{(i)}$ represents the electron-phonon coupling strength; $\theta(\omega)$ is the Heaviside step function.

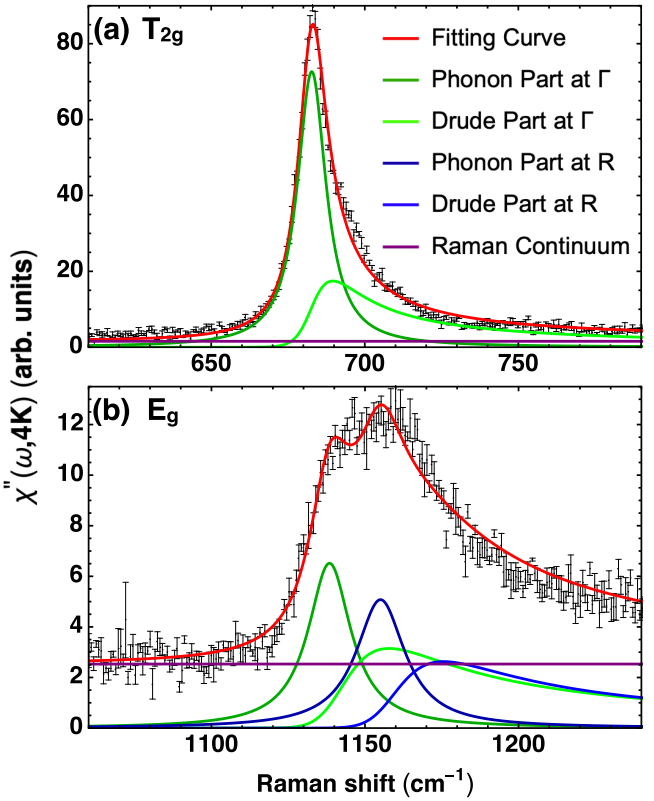

FIG. 11. The measured with 532 nm excitation at 4 K Raman response function (black points with one standard deviation error bars) fitted with the model of Eq. (11) for (a) the T_{2g} and (b) the E_g optical phonons coupled to low-frequency electronic excitations.

For the T_{2g} mode, we choose $\gamma_{D(\Gamma)}$ to be 3.0 cm^{-1}, which is consistent with the measured value of the T_{1g} quasielastic fluctuations at 16 K. For the E_g mode, we choose both $\gamma_{D(\Gamma)}$ and $\gamma_{D(R)}$ to be 11 cm^{-1}, which is consistent with the measured value of the A_{1g} quasielastic fluctuations at 16 K. We further require that $v_{(\Gamma)}$ and $v_{(R)}$ are the same.

The fitting results of the T_{2g} and E_g composite modes are shown in Fig. 11 and summarized in Table IV. The dip of the fitting curve in Fig. 11(b) results from the negligence of the contributions at k points between Γ and R points. The FWHM of the bare T_{2g} phonon mode (∼11 cm^{-1}) is similar to that of the A_{1g} phonon mode (∼12 cm^{-1}), while the FWHM of the bare E_g phonon mode (∼17 cm^{-1}) is larger. This large E_g FWHM, again, is an artifact caused by negligence of the contributions from the remaining k points. The energy difference between the E_g mode at Γ and R points is ∼17 cm^{-1}, which is comparable to the calculated difference of ∼30 cm^{-1} [72].

TABLE IV. The fitting parameters for the T_{2g} and E_g composite modes by Eq. (11). Units are given in the brackets.

Parameter (Units)	T_{2g} mode	E_g mode
$A_{(\Gamma)}$ (a.u.)	20.29 ± 0.03	7.4 ± 0.4
$\gamma_{L(\Gamma)}$ (cm^{-1})	5.67 ± 0.02	8.5 ± 0.5
$\omega_{L(\Gamma)}$ (cm^{-1})	682.73 ± 0.02	1138.4 ± 0.3
$A_{(R)}$ (a.u.)		7.0 ± 0.8
$\gamma_{L(R)}$ (cm^{-1})		10 ± 1
$\omega_{L(R)}$ (cm^{-1})		1155.0 ± 0.5
v (cm^{-1})	0.691 ± 0.005	2.2 ± 0.2

E. Quasielastic excitations

In Fig. 12 we show the symmetry-decomposed Raman response measured with 752 nm excitation at 300 K and 16 K. The low-energy Raman response shows quasielastic features which can be described by a Drude lineshape:

$$\chi''(\omega, T) \propto \frac{\alpha^2 \omega}{\omega^2 + \gamma^2}, \tag{12}$$

where α is the light-scattering vertex and γ measures the fluctuation rate.

The Raman response gets enhanced in all the channels on cooling. Especially, the T_{1g} Raman response changes qualitatively and develops into a strong quasielastic feature at low temperature. The basis functions of the T_{1g} representation in O_h group transform as the three components of angular momentum, which behave as a pseudovector [33]. This transformation property indicates that the observed quasielastic peak in T_{1g} channel may have a magnetic origin.

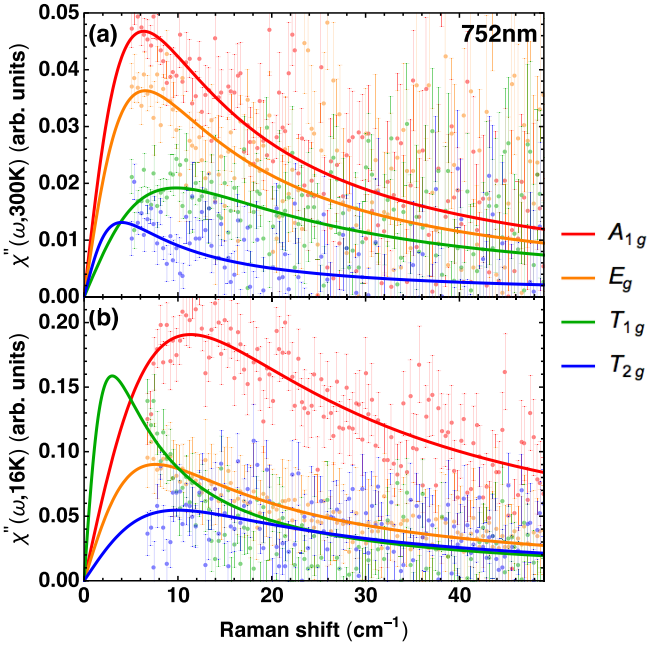

FIG. 12. Raman response $\chi''(\omega, T)$ in the four Raman-active symmetry channels measured with 752 nm excitation at (a) 300 K and (b) 16 K. The solid lines are Drude fits [Eq. (12)]. The error bars represent one standard deviation.

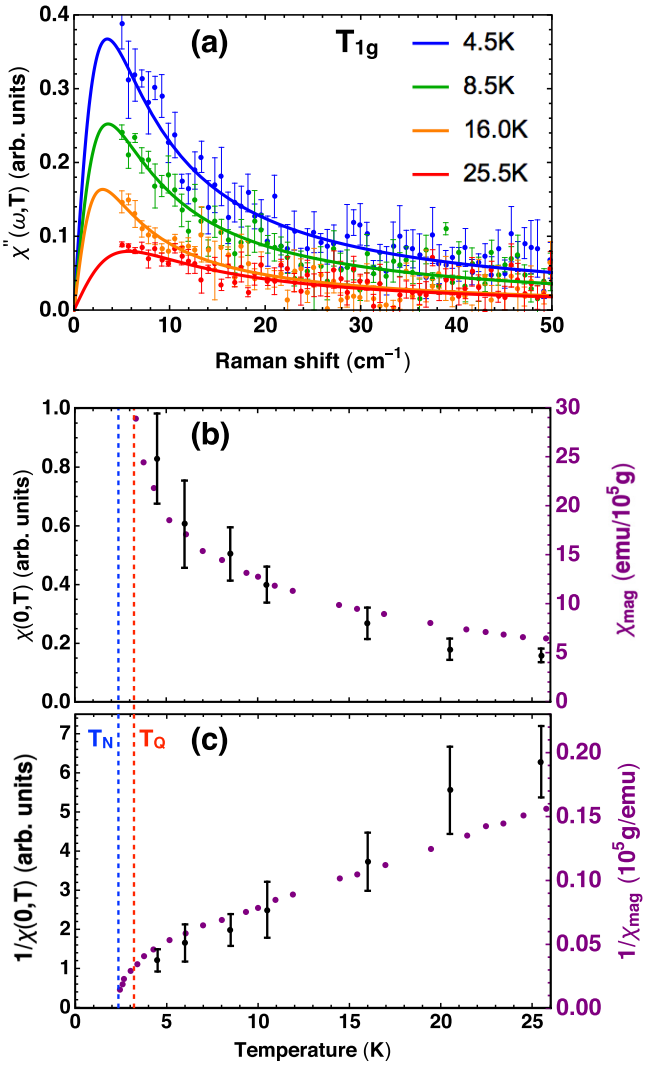

FIG. 13. (a) Temperature dependence of the Raman response $\chi''(\omega, T)$ in the T_{1g} symmetry channel measured with 752 nm excitation. The solid lines are Drude fits [Eq. (12)]. (b) Comparison between the temperature dependence of the static Raman susceptibility $\chi(0, T)$ (black) and that of the magnetic susceptibility χ_{mag} (purple) [75]. (c) Comparison between the temperature dependence of the inverse static Raman susceptibility (black) and that of the inverse magnetic susceptibility (purple) [75]. The blue arrow indicates the magnetic ordering temperature while the red one indicates the orbital ordering temperature. The error bars represent one standard deviation.

We measured the temperature dependence of Raman response in the XY scattering geometry, in which $T_{1g} + T_{2g}$ symmetry components are probed. Since T_{2g} signal at low-temperature is nearly constant [Fig. 12(b)], we fit the Raman response with the sum of Drude and constant terms and then remove the constant part to obtain the desired T_{1g} component [46]. The T_{1g} Raman response obtained this way is shown in Fig. 13(a). The quasielastic excitation in T_{1g} symmetry channel becomes significant below 20 K, and its intensity increases on further cooling. The static Raman susceptibility, $\chi(0, T)$, plotted in Fig. 13(b) is obtained from the Raman response by virtue of Kramers-Kronig relation:

$\chi(0,T) = \frac{2}{\pi}\int_0^{50\ cm^{-1}} \frac{\chi''(\omega,T)}{\omega} d\omega$. Drude function in Eq. (12) is used to extrapolate $\chi''(\omega, T)$ below 4 cm^{-1}. In Figs. 13(b) and 13(c), the temperature dependence of the static Raman susceptibility is compared with that of the magnetic susceptibility [75]. The fact that the temperature dependence of both quantities follows the same trend further supports the magnetic origin of the quasielastic peak in T_{1g} symmetry channel [76].

In zero magnetic field, Raman scattering data cannot determine whether the observed T_{1g} quasielastic response is of FM or AFM origin. Nevertheless, the Raman-measured T_{1g} quasielastic response is consistent with the FM correlations studied by INS: Without external magnetic field and above T_Q, the magnitude of the INS-measured zone-center quasielastic peak decreases on warming [29]. We note by passing that a first-principle calculation for CeB_6 indicates that the expected values of both $4f$-orbital occupancy and total angular momentum exhibit obvious anomalies around 20 K [77]. This is the same temperature around which the T_{1g} quasielastic Raman response starts to develop.

The mechanism responsible for the FM correlations can be understood as follows [26]. Consider the two electrons at neighboring Ce^{3+} sites. In the staggered orbital-ordering phase, the orbital part of the total wave function of these two electrons is antisymmetric. Due to the resulting exchange interaction, the spins at neighboring Ce^{3+} sites are FM correlated.

The Γ_8 CF ground state of O_h group has zero quadrupole moment. If the site symmetry is reduced from O_h group to D_{4h} group, the Γ_8 state of O_h group would be split into the Γ_6 and Γ_7 states of D_{4h} group. The Γ_6 and Γ_7 states can only have quadrupole moments of $x^2 - z^2$ or $y^2 - z^2$ type, rather than the proposed xy, yz, and zx type. Hence, only when the site symmetry is reduced to D_{2h} group, and the Γ_8 state of O_h group is split into two Γ_5 states of D_{2h} group, can the CF ground state carries finite quadrupole moments of xy, yz, and zx type. However, in a continuous second-order phase transition, the symmetry of the system cannot be directly reduced from cubic to orthorhombic, which violates Landau theory [78]. Theories which claim an AFQ phase with O_{xy}-type moments using a localized picture should address this difficulty. Inconsistency of the AFQ description has also been suggested based on magnetic-susceptibility anisotropy and magnetostriction measurements [79].

IV. CONCLUSION

In summary, we have employed optical secondary-emission spectroscopy to study the spin-orbital coupling (SOC), electronic crystal-field (CF) excitations, electron-phonon interaction, and long-wavelength magnetic fluctuations in the heavy-fermion metal CeB_6. Ce^{3+} ions have a single electron in the $4f$ shell. The SOC splits the degenerate $4f$ levels into a lower-energy $^2F_{5/2}$ multiplet and a higher-energy $^2F_{7/2}$ multiplet, with a separation of around 2000 cm^{-1}, from which we estimate the SOC strength $\xi = 610$ cm^{-1}.

The two multiplets are further split into five Kramers-degenerate CF states by the cubic CF potential. The $^2F_{5/2}$ multiplet is composed of one quartet Γ_8 ground state and one doublet Γ_7 excited state, and the $^2F_{7/2}$ multiplet consists of Γ_6^* and Γ_7^* doublets, and a Γ_8^* quartet states. We resolve all four electronic CF transitions: 380 cm^{-1} for the intramultiplet excitation, and 2060, 2200, and 2720 cm^{-1} for the three intermultiplet transitions.

On cooling, the FWHM for the $\Gamma_8 \rightarrow \Gamma_7$ and $\Gamma_8 \rightarrow \Gamma_7^*$ transitions first decreases from 300 K to 80 K but then increases below 80 K. We relate the decrease of the FWHM to lattice vibration driven fluctuations of the electrostatic potential at Ce sites, which diminish on cooling. The increase of the FWHM below 80 K results from the Kondo effect, an electron-correlation effect which increases the self-energy of the excited CF states. We apply a single-ion Hamiltonian model to obtain the eigenvalues and eigenfunctions of the $4f$-electron CF states. Using the Fermi golden rule, we also calculate the intensity of the four Raman active CF transitions and compare the calculation to the experimental data.

We study the lattice dynamics of CeB_6 and analyze the temperature dependence of all Raman active phonon modes. In the phonon spectra, we interpret the asymmetric lineshape of E_g and T_{2g} optical phonons as manifestation of electron-phonon interaction. We also identify a composite CF plus phonon excitation at 1158 cm^{-1}.

We acquire temperature dependence of the low-energy Raman response for all Raman-allowed symmetry channels and uncover the development of a quasielastic Raman response in the magnetic-dipolar T_{1g} symmetry channel below 20 K. The corresponding static Raman susceptibility shows similar temperature dependence as the magnetic susceptibility data, which supports the interpretation of its magnetic origin. By comparing the quasielastic Raman scattering data with electron spin resonance and inelastic neutron scattering results, we relate this T_{1g} spectral feature to ferromagnetic correlations.

Additionally, we detect photoluminescence emission centered at 1.95 eV at room temperature. We relate this emission to recombination of the electron-hole excitations between the $5d$ and $4f$ bands.

The experimental methods, models, and analyses demonstrated in this study can be applied to a range of systems, especially for rare-earth materials containing localized f electrons of Ce^{3+} or Yb^{3+} ions at high-symmetry crystallographic sites [80]. The approach could enable us to probe ferroquadrupolar (FQ) fluctuations in $TmAg_2$ ($T_{FQ} = 5.0$ K) [11] or $TmAu_2$ ($T_{FQ} = 7.0$ K) [12] systems, to name a few examples. Also, magnetic correlation induced by quadrupolar ordering could be probed in antiferroquadrupolar (AFQ) systems, for instance in UPd_3 (multiple AFQ phases, with the highest $T_{AFQ} = 7.6$ K) [81], NpO_2 ($T_{AFQ} = 25.0$ K) [14], or DyB_2C_2 ($T_{AFQ} = 24.7$ K) [13].

ACKNOWLEDGMENTS

We are grateful to K. Haule and P. Coleman for discussions. We thank A. Lee for participating in the early data acquisition. The spectroscopic work at Rutgers (M.Y., H.-H.K, G.B.) was supported by NSF Grant No. DMR-1709161. Sample synthesis at Los Alamos was performed under the auspices of the U.S. Department of Energy, Office of Basic Energy Sciences, Division of Materials Science and Engineering. G.B. also

acknowledges the QuantEmX grant from ICAM, the Gordon and Betty Moore Foundation through Grant No. GBMF5305 allowing G.B. to make a collaborative visit to Stanford. Work at NICBP was supported by IUT23-3 grant.

[1] M. Imada, A. Fujimori, and Y. Tokura, Metal-insulator transitions, Rev. Mod. Phys. **70**, 1039 (1998).

[2] E. Dagotto, Complexity in strongly correlated electronic systems, Science **309**, 257 (2005).

[3] K. T. Moore and G. van der Laan, Nature of the $5f$ states in actinide metals, Rev. Mod. Phys. **81**, 235 (2009).

[4] C. Pfleiderer, Superconducting phases of f-electron compounds, Rev. Mod. Phys. **81**, 1551 (2009).

[5] Y. Kuramoto, H. Kusunose, and A. Kiss, Multipole orders and fluctuations in strongly correlated electron systems, J. Phys. Soc. Jpn. **78**, 072001 (2009).

[6] P. Santini, S. Carretta, G. Amoretti, R. Caciuffo, N. Magnani, and G. H. Lander, Multipolar interactions in f-electron systems: The paradigm of actinide dioxides, Rev. Mod. Phys. **81**, 807 (2009).

[7] A. S. Cameron, G. Friemel, and D. S. Inosov, Multipolar phases and magnetically hidden order: Review of the heavy-fermion compound $Ce_{1-x}La_xB_6$, Rep. Prog. Phys. **79**, 066502 (2016).

[8] M.-T. Suzuki, H. Ikeda, and P. M. Oppeneer, First-principles theory of magnetic multipoles in condensed matter systems, J. Phys. Soc. Jpn. **87**, 041008 (2018).

[9] D. L. Cox, Quadrupolar Kondo Effect in Uranium Heavy-Electron Materials? Phys. Rev. Lett. **59**, 1240 (1987).

[10] H. Kotegawa, M. Yogi, Y. Imamura, Y. Kawasaki, G.-Q. Zheng, Y. Kitaoka, S. Ohsaki, H. Sugawara, Y. Aoki, and H. Sato, Evidence for Unconventional Strong-Coupling Superconductivity in $PrOs_4Sb_{12}$: An Sb Nuclear Quadrupole Resonance Study, Phys. Rev. Lett. **90**, 027001 (2003).

[11] P. Morin and J. Rouchy, Quadrupolar ordering in tetragonal $TmAg_2$, Phys. Rev. B **48**, 256 (1993).

[12] M. Kosaka, H. Onodera, K. Ohoyama, M. Ohashi, Y. Yamaguchi, S. Nakamura, T. Goto, H. Kobayashi, and S. Ikeda, Quadrupolar ordering and magnetic properties of tetragonal $TmAu_2$, Phys. Rev. B **58**, 6339 (1998).

[13] K. Hirota, N. Oumi, T. Matsumura, H. Nakao, Y. Wakabayashi, Y. Murakami, and Y. Endoh, Direct Observation of Antiferroquadrupolar Ordering: Resonant X-Ray Scattering Study of DyB_2C_2, Phys. Rev. Lett. **84**, 2706 (2000).

[14] J. A. Paixão, C. Detlefs, M. J. Longfield, R. Caciuffo, P. Santini, N. Bernhoeft, J. Rebizant, and G. H. Lander, Triple-$\vec{q}$ Octupolar Ordering in NpO_2, Phys. Rev. Lett. **89**, 187202 (2002).

[15] M. Tsujimoto, Y. Matsumoto, T. Tomita, A. Sakai, and S. Nakatsuji, Heavy-Fermion Superconductivity in the Quadrupole Ordered State of PrV_2Al_{20}, Phys. Rev. Lett. **113**, 267001 (2014).

[16] A. Takase, K. Kojima, T. Komatsubara, and T. Kasuya, Electrical resistivity and magnetoresistance of CeB_6, Solid State Commun. **36**, 461 (1980).

[17] T. Fujita, M. Suzuki, T. Komatsubara, S. Kunii, T. Kasuya, and T. Ohtsuka, Anomalous specific heat of CeB_6, Solid State Commun. **35**, 569 (1980).

[18] P. Burlet, J. Rossat-Mignod, J. M. Effantin, T. Kasuya, S. Kunii, and T. Komatsubara, Magnetic ordering in cerium hexaboride CeB_6, J. Appl. Phys. **53**, 2149 (1982).

[19] O. Zaharko, P. Fischer, A. Schenck, S. Kunii, P.-J. Brown, F. Tasset, and T. Hansen, Zero-field magnetic structure in CeB_6 reinvestigated by neutron diffraction and muon spin relaxation, Phys. Rev. B **68**, 214401 (2003).

[20] H. Nakao, K.-i. Magishi, Y. Wakabayashi, Y. Murakami, K. Koyama, K. Hirota, Y. Endoh, and S. Kunii, Antiferroquadrupole ordering of CeB_6 studied by resonant x-ray scattering, J. Phys. Soc. Jpn. **70**, 1857 (2001).

[21] S. Nakamura, T. Goto, S. Kunii, K. Iwashita, and A. Tamaki, Quadrupole-strain interaction in rare earth hexaborides, J. Phys. Soc. Jpn. **63**, 623 (1994).

[22] K. Hanzawa, Hyperfine Interactions in CeB_6, J. Phys. Soc. Jpn. **69**, 510 (2000).

[23] K. Kunimori, M. Sera, H. Tanida, T. Matsumura, and F. Iga, New type of the domain-redistribution at low magnetic fields in phase II of CeB_6, J. Phys. Soc. Jpn. **81**, 104706 (2012).

[24] T. Matsumura, T. Yonemura, K. Kunimori, M. Sera, and F. Iga, Magnetic Field Induced $4f$ Octupole in CeB_6 Probed by Resonant X-Ray Diffraction, Phys. Rev. Lett. **103**, 017203 (2009).

[25] T. Matsumura, T. Yonemura, K. Kunimori, M. Sera, F. Iga, T. Nagao, and J.-I. Igarashi, Antiferroquadrupole order and magnetic field induced octupole in CeB_6, Phys. Rev. B **85**, 174417 (2012).

[26] P. Schlottmann, Electron spin resonance in antiferroquadrupolar-ordered CeB_6, Phys. Rev. B **86**, 075135 (2012).

[27] S. V. Demishev, A. V. Semeno, A. V. Bogach, N. A. Samarin, T. V. Ishchenko, V. B. Filipov, N. Yu. Shitsevalova, and N. E. Sluchanko, Magnetic spin resonance in CeB_6, Phys. Rev. B **80**, 245106 (2009).

[28] P. Y. Portnichenko, S. V. Demishev, A. V. Semeno, H. Ohta, A. S. Cameron, M. A. Surmach, H. Jang, G. Friemel, A. V. Dukhnenko, N. Yu. Shitsevalova, V. B. Filipov, A. Schneidewind, J. Ollivier, A. Podlesnyak, and D. S. Inosov, Magnetic field dependence of the neutron spin resonance in CeB_6, Phys. Rev. B **94**, 035114 (2016).

[29] H. Jang, G. Friemel, J. Ollivier, A. V. Dukhnenko, N. Yu Shitsevalova, V. B. Filipov, B. Keimer, and D. S. Inosov, Intense low-energy ferromagnetic fluctuations in the antiferromagnetic heavy-fermion metal CeB_6, Nat. Mater. **13**, 682 (2014).

[30] T. Takahashi, T. Morimoto, T. Yokoya, S. Kunii, T. Komatsubara, and O. Sakai, Crystal-field splitting in CeB_6 as observed by high-resolution photoemission, Phys. Rev. B **52**, 9140 (1995).

[31] A. Koitzsch, N. Heming, M. Knupfer, B. Buchner, P. Y. Portnichenko, A. V. Dukhnenko, N. Y. Shitsevalova, V. B. Filipov, L. L. Lev, V. N. Strocov, J. Ollivier, and D. S. Inosov, Nesting-driven multipolar order in CeB_6 from photoemission tomography, Nat. Commun. **7**, 10876 (2016).

[32] Photoemission spectroscopy probes energy states below the Fermi level, thus ARPES cannot directly access the $^2F_{7/2}$ multiplet. However, virtual excitations to the narrow $^2F_{7/2}$ multiplet contribute to the self energy of the spectral function, making the

$^2F_{7/2}$ multiplet identifiable in the photoemission spectra. Details of this mechanism can be found in Refs. [82,83,84].

[33] G. F. Koster, *Properties of the Thirty-Two Point Groups* (M.I.T. Press, Cambridge, 1963).

[34] Asterisks are used to distinguish the CF states of the $^2F_{7/2}$ multiplet (Γ_6^*, Γ_7^*, and Γ_8^*) from those of the $^2F_{5/2}$ multiplet (Γ_7 and Γ_8).

[35] N. Sato, S. Kunii, I. Oguro, T. Komatsubara, and T. Kasuya, Magnetic properties of single crystals of $Ce_xLa_{1-x}B_6$, J. Phys. Soc. Jpn. **53**, 3967 (1984).

[36] E. Zirngiebl, B. Hillebrands, S. Blumenröder, G. Güntherodt, M. Loewenhaupt, J. M. Carpenter, K. Winzer, and Z. Fisk, Crystal-field excitations in CeB_6 studied by Raman and neutron spectroscopy, Phys. Rev. B **30**, 4052(R) (1984).

[37] O. Sakai, R. Shiina, H. Shiba, and P. Thalmeier, A new interpretation of NMR in quadrupolar ordering phase of CeB_6 - consistency with neutron scattering, J. Phys. Soc. Jpn. **66**, 3005 (1997).

[38] M. Sundermann, K. Chen, H. Yavaş, H. Lee, Z. Fisk, M. W. Haverkort, L. H. Tjeng, and A. Severing, The quartet ground state in CeB_6: An inelastic x-ray scattering study, Europhys. Lett. **117**, 17003 (2017).

[39] M. Loewenhaupt, J. M. Carpenter, and C. K. Loong, Magnetic excitations in CeB_6, J. Magn. Magn. Mater. **52**, 245 (1985).

[40] W. Hayes and R. Loudon, *Scattering of Light by Crystals* (Dover Publications, London, 2004).

[41] G. Schaack, Raman scattering by crystal-field excitations, in *Light Scattering in Solids VII*, edited by M. Cardona and G. Güntherodt (Springer, Berlin, 2000), pp. 30–179.

[42] G. Güntherodt, E. Zirngiebl, R. Mock, H. Brenten, S. Blumenröder, G. Pofahl, and Z. Fisk, Raman and brillouin scattering spectroscopy of intermediate valence and heavy fermion compounds, in *Theoretical and Experimental Aspects of Valence Fluctuations and Heavy Fermions*, edited by L. C. Gupta and S. K. Malik (Springer, Boston, 1987), pp. 261–268.

[43] N. Foroozani, J. Lim, G. Fabbris, P. F. S. Rosa, Z. Fisk, and J. S. Schilling, Suppression of dense Kondo state in CeB_6 under pressure, Physica B (Amsterdam) **457**, 12 (2015).

[44] P. C. Canfield and Z. Fisk, Growth of single crystals from metallic fluxes, Philos. Mag. B **65**, 1117 (1992).

[45] We mainly followed the procedure discussed in Ref. [85] to estimate the laser heating. The optical absorption coefficient data were extracted from the optical data [47–49], while the thermal conductivity data were taken from Ref. [86].

[46] See Supplemental Material at http://link.aps.org/supplemental/10.1103/PhysRevMaterials.3.065003 for details of analysis of Raman data and for calculation of the crystal field state eigenfunctions, which includes Refs. [40,87–90].

[47] S. Kimura, T. Nanba, S. Kunii, T. Suzuki, and T. Kasuya, Anomalous infrared absorption in rare-earth hexaborides, Solid State Commun. **75**, 717 (1990).

[48] S. Kimura, T. Nanba, M. Tomikawa, S. Kunii, and T. Kasuya, Electronic structure of rare-earth hexaborides, Phys. Rev. B **46**, 12196 (1992).

[49] S.-I. Kimura, T. Nanba, S. Kunii, and T. Kasuya, Low-energy optical excitation in rare-earth hexaborides, Phys. Rev. B **50**, 1406 (1994).

[50] M. Kitamura, $4f$ levels of rare-earth hexaborides: A simple approach based on a modified orthogonalized-plane-wave method and a self-consistent-field atomic-structure calculation, Phys. Rev. B **49**, 1564 (1994).

[51] M. B. Suvasini, G. Y. Guo, W. M. Temmerman, G. A. Gehring, and M. Biasini, The Fermi surface of CeB_6, J. Phys.: Condens. Matter **8**, 7105 (1996).

[52] M. Neupane, N. Alidoust, I. Belopolski, G. Bian, S.-Y. Xu, D.-J. Kim, P. P. Shibayev, D. S. Sanchez, H. Zheng, T.-R. Chang, H.-T. Jeng, P. S. Riseborough, H. Lin, A. Bansil, T. Durakiewicz, Z. Fisk, and M. Z. Hasan, Fermi surface topology and hot spot distribution in the Kondo lattice system CeB_6, Phys. Rev. B **92**, 104420 (2015).

[53] The energy of the $\Gamma_8 \rightarrow \Gamma_7$ transition shows monotonic temperature dependence. The earlier reports, Refs. [36,39], showed no temperature dependence of the transition energy on cooling from 300 K to 20 K, followed by a rapidly hardening on cooling below 20 K.

[54] G. S. Nolas, V. G. Tsoukala, S. K. Gayen, and G. A. Slack, Electronic-raman-scattering study of the low-lying energy levels of trivalent cerium-doped yttria, Phys. Rev. B **50**, 150 (1994).

[55] G. M. Williams, P. C. Becker, J. G. Conway, N. Edelstein, L. A. Boatner, and M. M. Abraham, Intensities of electronic Raman scattering between crystal-field levels of Ce^{3+} in $LuPO_4$: Nonresonant and near-resonant excitation, Phys. Rev. B **40**, 4132 (1989).

[56] A. C. Hewson, *The Kondo Problem To Heavy Fermions* (Cambridge University Press, Cambridge, 1993).

[57] M. Ya. Amusia, K. G. Popov, V. R. Shaginyan, and V. A. Stephanovich, *Theory of Heavy-Fermion Compounds* (Springer, Switzerland, 2015).

[58] C. Terzioglu, D. A. Browne, R. G. Goodrich, A. Hassan, and Z. Fisk, EPR and magnetic susceptibility measurements on CeB_6, Phys. Rev. B **63**, 235110 (2001).

[59] K. R. Lea, M. J. M. Leask, and W. P. Wolf, The raising of angular momentum degeneracy of f-electron terms by cubic crystal fields, J. Phys. Chem. Solids **23**, 1381 (1962).

[60] K. W. H. Stevens, Matrix elements and operator equivalents connected with the magnetic properties of rare earth ions, Proc. Phys. Soc. A **65**, 209 (1952).

[61] When comparing the CF coefficients across different literature, additional constants are needed [91,92].

[62] K. Tanaka and Y. Ōnuki, Observation of $4f$ electron transfer from Ce to B_6 in the Kondo crystal CeB_6 and its mechanism by multi-temperature X-ray diffraction, Acta Crystallogr. Sect. B **58**, 423 (2002).

[63] T. P. Devereaux and R. Hackl, Inelastic light scattering from correlated electrons, Rev. Mod. Phys. **79**, 175 (2007).

[64] J. D. Axe, Two-photon processes in complex atoms, Phys. Rev. **136**, A42 (1964).

[65] A. Kiel, T. Damen, S. P. S. Porto, S. Singh, and F. Varsanyi, Electronic raman effect in paramagnetic crystals: $CeCl_3$, Phys. Rev. **178**, 1518 (1969).

[66] E. Zirngiebl, S. Blumenröder, R. Mock, and G. Güntherodt, Relation of phonon anomalies to charge fluctuation rates in intermediate valence compounds, J. Magn. Magn. Mater. **54-57**, 359 (1986).

[67] N. Ogita, S. Nagai, N. Okamoto, M. Udagawa, F. Iga, M. Sera, J. Akimitsu, and S. Kunii, Raman scattering investigation of

RB_6 (R = Ca, La, Ce, Pr, Sm, Gd, Dy, and Yb), Phys. Rev. B **68**, 224305 (2003).

[68] S. Kunii, J. M. Effantin, and J. Rossat-Mingnod, Lattice dynamics in CeB_6 studied by neutron-scattering and specific-heat measurements, J. Phys. Soc. Jpn. **66**, 1029 (1997).

[69] T. Livneh, Coupling of multi-LO phonons to crystal-field excitations in UO_2 studied by Raman spectroscopy, J. Phys.: Condens. Matter **20**, 085202 (2008).

[70] R. F. Wallis, I. P. Ipatova, and A. A. Maradudin, Temperature dependence of the width of the fundamental lattice-vibration absorption peak in ionic crystals, Sov. Phys. Solid State **8**, 850 (1966).

[71] M. Balkanski, R. F. Wallis, and E. Haro, Anharmonic effects in light scattering due to optical phonons in silicon, Phys. Rev. B **28**, 1928 (1983).

[72] T. Gürel and R. Eryiğit, *Ab initio* lattice dynamics and thermodynamics of rare-earth hexaborides LaB_6 and CeB_6, Phys. Rev. B **82**, 104302 (2010).

[73] There are other constraints which the decay processes must satisfy. For example, the spontaneous decay of a phonon by anharmonic processes of any order into a set of phonons of higher phase velocity is impossible [93].

[74] Because in CeB_6 the maximum acoustic phonon frequency is around 100 cm^{-1}, for the high-frequency A_{1g} mode decay into two acoustic modes is impossible.

[75] M. Kawakami, S. Kunii, T. Komatsubara, and T. Kasuya, Magnetic properties of CeB_6 single crystal, Solid State Commun. **36**, 435 (1980).

[76] H.-H. Kung, R. E. Baumbach, E. D. Bauer, V. K. Thorsmølle, W.-L. Zhang, K. Haule, J. A. Mydosh, and G. Blumberg, Chirality density wave of the "hidden order" phase in URu_2Si_2, Science **347**, 1339 (2015).

[77] H. Lu and L. Huang, Anomaly in the temperature-dependent electronic structure of the heavy-fermion compound CeB_6: A theoretical investigation by means of a first-principles many-body approach, Phys. Rev. B **95**, 155140 (2017).

[78] L. D. Landau and E. M. Lifshitz, Chapter XIV - phase transitions of the second kind and critical phenomena, in *Statistical Physics*, 3rd ed. (Butterworth-Heinemann, Oxford, 1980), pp. 446–516.

[79] M. Amara and R.-M. Galéra, CeB_6 Macroscopically Revisited, Phys. Rev. Lett. **108**, 026402 (2012).

[80] M. Ye, E. W. Rosenberg, I. R. Fisher, and G. Blumberg, Lattice dynamics, crystal-field excitations and quadrupolar fluctuations of $YbRu_2Ge_2$, Phys. Rev. B **99**, 235104 (2019).

[81] N. Lingg, D. Maurer, V. Müller, and K. A. McEwen, Ultrasound investigations of orbital quadrupolar ordering in UPd_3, Phys. Rev. B **60**, R8430 (1999).

[82] O. Gunnarsson and K. Schönhammer, Electron spectroscopies for Ce compounds in the impurity model, Phys. Rev. B **28**, 4315 (1983).

[83] P. Coleman, New approach to the mixed-valence problem, Phys. Rev. B **29**, 3035 (1984).

[84] F. Patthey, W. D. Schneider, Y. Baer, and B. Delley, High-Temperature Collapse of the Kondo Resonance in $CeSi_2$ Observed by Photoemission, Phys. Rev. Lett. **58**, 2810 (1987).

[85] A. A. Maksimov, A. V. Puchkov, I. I. Tartakovskii, V. B. Timofeev, D. Reznik, and M. V. Klein, Investigations of the temperature dependence of the low energy electronic Raman scattering in $Tl_2Ba_2CaCu_2O_8$ single crystals, Solid State Commun. **81**, 407 (1992).

[86] M. Sera, S. Kobayashi, M. Hiroi, N. Kobayashi, and S. Kunii, Thermal conductivity of RB_6 (R = Ce, Pr, Nd, Sm, Gd) single crystals, Phys. Rev. B **54**, R5207 (1996).

[87] R. Loudon, The Raman effect in crystals, Adv. Phys. **13**, 423 (1964).

[88] M. V. Klein, Theory of two-phonon Raman scattering in transition metals and compounds, Phys. Rev. B **24**, 4208 (1981).

[89] P. Nyhus, S. L. Cooper, Z. Fisk, and J. Sarrao, Low-energy excitations of the correlation-gap insulator SmB_6: A light-scattering study, Phys. Rev. B **55**, 12488 (1997).

[90] P. Fazekas, *Lecture Notes on Electron Correlation and Magnetism* (World Scientific Publishing, Singapore, 1999).

[91] M. T. Hutchings, Point-Charge Calculations of Energy Levels of Magnetic Ions in Crystalline Electric Fields, Solid State Phys. **16**, 227 (1964).

[92] A. J. Kassman, Relationship between the coefficients of the tensor operator and operator equivalent methods, J. Chem. Phys. **53**, 4118 (1970).

[93] M. Lax, P. Hu, and V. Narayanamurti, Spontaneous phonon decay selection rule: N and U processes, Phys. Rev. B **23**, 3095 (1981).